Fracture resistant bones: unusual deformation mechanisms of seahorse armor

Michael M Porter[1*], Ekaterina Novitskaya[1], Ana Bertha Castro-Ceseña[1], Marc A Meyers[1,2,3], Joanna McKittrick[1,2]

[1]*Materials Science and Engineering Program, University of California, San Diego.*
[2]*Department of Mechanical and Aerospace Engineering, University of California, San Diego.*
[3]*Department of NanoEngineering, University of California, San Diego.*

**Correspondence to: Michael M Porter - Email: m1porter@ucsd.edu; Tel.: 1-757-615-3929; Fax: 1-858-534-5698.*

Abstract

Multifunctional materials and devices found in nature serve as inspiration for advanced synthetic materials, structures, and robotics. Here, we elucidate the structural mechanics and unusual deformation mechanisms discovered in seahorses that provide them prehension and protection against predators. The seahorse tail is composed of subdermal bony plates arranged in articulating ring-like segments that overlap for controlled ventral bending and twisting. The bony plates are fracture resistant materials designed to slide past one another and buckle when compressed. This complex plate and segment motion, along with the unique hardness distribution and architectural hierarchy of each plate, provide seahorses joint flexibility while shielding them against impact and crushing. Mimicking seahorse armor may lead to novel biomimetic technologies, such as flexible armor, fracture resistant structures, or prehensile robotics.

Keywords: seahorse; natural armor; prehensile; bony plates

1. Introduction

Recent interest in biomimicry and bio-inspired design has led to a renewed study of biological materials and devices [1, 2]. Nature offers a plethora of functional designs, ranging from spider silk to insect flight, that inspire materials scientists and engineers to develop new, high-performance materials, structures, and robotic devices [2-4]. In a quest to discover novel, multifunctional defense mechanisms that exist in nature, we investigated the structure-property-function relationships of the bony-plated armor in the seahorse, *Hippocampus kuda*.

Seahorses, known for their equine profile and vertical swimming posture, are remarkable fish with a variety of unique characteristics that comprise the genus *Hippocampus*, family Syngnathidae. They have a head like a horse, a long tubular snout like an anteater, eyes that move independently like a chameleon, a brood pouch like a kangaroo, camouflage skin like a flounder, and a flexible prehensile tail like a monkey [5, 6]. Unlike most fish, seahorses have no caudal fin and swim upright with a single dorsal fin for propulsion and two pectoral fins for maneuverability [7, 8]. This unique posture, their cryptic appearance, and their ability to suction feed and grasp objects allow these slow swimmers to thrive in obstacle-strewn sea grasses, mangroves, and coral reefs [5, 6]. Although seahorses primarily rely on camouflage skin and dermal excrescences (e.g., filamentous or polyp-like growths) to avoid predators [5, 6], they have also evolved a segmented array of bony plates that functions as a flexible, subdermal armor [9, 10].

Natural armor in most marine animals such as bony fish, crustaceans, and mollusks often exists in the form of external scales, exoskeletons, and shells [11-13]. These natural materials are typically rigid, mineralized structures designed for body support and environmental protection [11-13]. Seahorses, in contrast to most teleosts, have internal bony plates instead of scales, arranged in articulating ring-like segments spanning the length of the fish (Fig. 1). The bony plates not only provide seahorses body support and protection, but also the ability to bend their tails to grasp and hold objects [9, 10].

Most natural armor in fish limits axial bending [14, 15] - a necessary tradeoff for the protection it provides. However, Hale [9] and Praet et al. [10] argue that the bony plates in seahorses play an essential role in axial bending and the prehensility of their tails. In fact, seahorses can precisely control body movements to twist and bend ventrally; motions usually disadvantageous in laterally swimming fish [9]. The body plating provides a rigid structure for myomere muscles to pull on and transmit forces to the vertebrae [9, 10]. In the tail, the hypaxial muscles are oriented vertically connecting the ventral plates to the horizontal septa of the vertebrae, while the epaxial muscles are oriented concentrically connecting the dorsal plates to the vertebrae [10]. This is very different from most teleost, whose muscles are all oriented concentrically and pull directly on the vertebrae, with thick collagen fibers in the skin that limit body twisting and ventral bending [9, 14, 16]. Beyond muscular force transmission and body mobility, the bony plates play a defensive role as protective armor. The bony armor must be mechanically hard and sufficiently tough to resist fracture from impact and crushing, yet elastic and flexible enough for controlled axial bending and prehension.

The mechanisms of plate and segment motion, the architectural hierarchy and the mechanical properties of the bony-plated armor that protect seahorses are revealed here through micro-computed tomography (μCT), scanning electron microscopy (SEM), and mechanical testing. The overlapping architectural arrangement of the bony plates and segments are shown to allow significant deformations without fracture, protecting the spinal column from failure. The material composition, microstructural features, and hardness of the bony plates were investigated

and compared to that of other natural materials, including fish scales, crab exoskeleton, and abalone nacre. Mimicking the multifunctional bony-plated armor of the seahorse tail may lead to new bio-inspired technologies.

2. Materials and Methods

2.1. Sample collection and preparation

Several seahorse specimens of *Hippocampus kuda* were donated by the Birch Aquarium at Scripps Institute of Oceanography, University of California, San Diego on October 2011. The seahorses were confiscated alive in Bali, Indonesia on October 2005 and died, due to stress, during transport to the aquarium where they were kept frozen. The specimens were thawed and preserved by immersing them in 70% isopropanol at room temperature prior to analysis.

2.2. Material composition

The mineral, protein, and water fractions of the seahorse bones were measured by weight. The initially hydrated bones were cleaned under an optical microscope to remove any connective tissues and weighed. The untreated bones were then freeze-dried for 12 hr with a FreeZone benchtop lyophilizer (Labconco, Kansas City, MO) and weighed to determine the water content. After dehydration, approximately 0.5 g of untreated bones were immersed in 12 mL of 12.5% NaClO for complete deproteinization. The deproteinated samples were then freeze-dried for 12 hr and weighed. The water, mineral, and protein fractions of the seahorse bones were calculated by Eq. 1-3:

$$x_{water} = \left(1 - \frac{m_{dry}}{m_{initial}}\right) \times 100\% \qquad (1)$$

$$x_{mineral} = \left(\frac{m_{mineral}}{m_{initial}}\right) \times 100\% \qquad (2)$$

$$x_{protein} = \left(\frac{m_{dry} - m_{mineral}}{m_{initial}}\right) \times 100\% \qquad (3)$$

where x_i is the weight percent (wt%) of component i - water, mineral, and protein - and m_j is the measured mass of component j - initial hydrated sample, dry untreated sample, and deproteinated mineral sample, respectively.

2.3. Compression testing

Tail sections cut from the base (torso-tail intersection) of several mature seahorse tails, containing three bony segments per tail section, were cut and loaded in compression with an Instron materials testing machine (Instron 3367, Norwood, MA) with a 30 kN load cell at a crosshead velocity of 10^{-3} mm/sec. The tail sections were compressed to ~60% strain in three orthogonal directions: (i) laterally; (ii) ventral-dorsally; (iii) distal-proximally. The specimens remained hydrated with 70% isopropanol during each test. The measured dimensions of the tail sections were approximately $7 \times 7 \times 10$ mm^3, rounded to the nearest 0.5 mm. Representative stress-strain curves were plotted from the measured force-displacement and estimated cross-sectional areas for comparison.

2.4. Micro-hardness testing

Micro-hardness of the bony plates was measured using a LECO M-400-H1 hardness testing machine equipped with a Vickers hardness indenter. Four dorsal plates excised from two tail segments cut from the base (torso-tail intersection) of a mature seahorse tail were cleaned, embedded in epoxy resin and polished until the surfaces of the samples were exposed. The embedded bony plates were positioned such that four different locations of each plate could be tested to determine the overall hardness distribution across a single bony plate. Hardness values at the four different locations were averaged from 16 micro-indentations each. The surface hardness of several bony plates along the length of the tail was measured to confirm that the hardness remained constant along the length. The hardness of the interior and exterior of several bony plate cross-sections were also measured. A load of 100 gf was used to indent the exposed surfaces. The Vickers hardness of the bony plates was evaluated by Eq. 4:

$$HV = \left(1.854 \frac{F}{d^2}\right) \times 9.81 \qquad (4)$$

where HV is the Vicker's hardness number in MPa, F is the applied load in kgf, and d is the arithmetic mean of the two measured diagonals in mm.

2.5. Micro-computed tomography (μCT)

An infant seahorse, ~6 months old, immersed in 70% isopropanol, one dried tail section composed of three bony-plated segments, three dried tail sections compressed in different orientations, and one dried bony plate excised from the left dorsal side of a mature seahorse tail were scanned on a micro-computed tomography (μCT) scanner, Skyscan 1076 (Kontich, Belgium). For sample preparation, the seahorse was wrapped in a kimwipe moistened with a phosphate buffer saline (PBS) solution and placed in a sealed tube to prevent the specimen from drying out during scanning. The four tail sections and the bony plate were scanned inside dry plastic tubes. Imaging was performed at 36 μm isotropic voxel size for the seahorse and 9 μm isotropic voxel sizes for the tail sections and bony plate. An electric potential of 70 kVp and a

current of 200 µA was applied using a 0.5 mm aluminum filter. A beam hardening correction algorithm was applied during image reconstruction of all samples. Images and 3-dimensional rendered models were developed using Skyscan's Dataviewer and CTVox software.

2.6. Scanning electron microscopy (SEM)

Prior to imaging the bones were cleaned under an optical microscope, washed with deionized water, then dried in a desiccant for 48 hr, and sputter-coated with iridium using an Emitech K575X sputter coater (Quorum Technologies Ltd., West Sussex, UK). Both fully intact and fracture surfaces of the specimens were imaged at 5 kV with a Philips XL30 field emission environmental scanning electron microscope (ESEM) (FEI-XL30, FEI Company, Hillsboro, OR).

3. Results and Discussion

Fig. 1 shows µCT images of a seahorse skeleton (*Hippocampus kuda*), illustrating the morphology of several ring-like segments, each composed of plates surrounding a single vertebra, at different locations along the fish. The torso is supported by a scaffold of ~11 heptagonal segments (Fig. 1a-c). At the dorsal fin (torso-tail intersection) the segments become hexagonal (Fig. 1d), and then square (Fig. 1e). The prehensile tail has ~36 square-like segments (Fig. 1e), each composed of four corner plates that decrease linearly in size along the length of the tail. The plates and vertebrae are joined by thick, subdermal collagen layers of connective tissue and free to glide or pivot depending on the particular design of each joint. Praet et al. [10] identified eight gliding joints and five pivoting (ball-and-socket) joints per tail segment.

Figure 2 shows the architectural arrangement of the different bones (Fig. 2a) and joints (Fig. 2b) in the tail. Adjacent bony plates in each tail segment overlap at the dorsal, ventral, and lateral midlines (Fig. 2c) [9, 10]. There are four gliding joints per segment with this configuration. On both the dextral and sinistral sides of the tail, the ventral plates always overlap the dorsal plates [10]. Conversely, the dextral-sinistral or sinistral-dextral overlaps on the dorsal and ventral sides of the tail are randomly sequenced from segment to segment, and may be distinct to each individual seahorse, much like the uniqueness of their cranial coronets [5]. Each ring of bony plates overlaps its anterior neighbor to permit axial bending (see Fig. 2b). Neighboring segments are connected by four gliding joints where the distal spines of the anterior plates insert into the proximal grooves of the posterior plates (Fig. 2d) [9, 10]. Even though the soft connective tissue provides these joints some rotational and translational freedom, the gliding motion of the plates is predominantly restricted to one translational degree of freedom (see arrows in Fig. 2c and 2d). Successive vertebrae, on the other hand, are connected by pivoting joints with three rotational degrees of freedom (Fig. 2e) [10]. Each vertebra is joined to the bony plates by connective tissue attached to the vertebral struts at the dorsal, ventral, and lateral midlines (Fig. 2f) [10]. The plate-vertebra junctions are extremely flexible joints with nearly six

degrees of freedom: three rotational (pivoting) and three translational (gliding) - although translational motion is fairly limited [10]. This complex mechanism of plate and segment motion, regulated by collagenous connective tissue, allows seahorses to bend their tails ventrally in a logarithmic spiral/helicoidal fashion. Slight lateral bending can occur concurrently with ventral bending; however, the regular ventral-dorsal overlaps and random lateral overlaps seem to prevent significant lateral bending [9].

Figure 3 contains results from compression tests on hydrated seahorse tail sections (each composed of three bony segments). The tail sections were compressed to ~60% strain in three orthogonal directions: (i) laterally (dextral-sinistrally), (ii) ventral-dorsally, and (iii) distal-proximally. As seen in the stress-strain plot (Fig. 3a), the tail exhibits an anisotropic response to compressive loading and $\partial^2\sigma/\partial\varepsilon^2 > 0$ (σ = stress; ε = stain) indicating that it becomes progressively more difficult to deform the tail as the stress increases. Fig. 3b and 3c show µCT images of the distal and dorsal views of a seahorse tail section before compression. When compressed laterally (Fig. 3i), the stress response is minimal and the lateral struts of the vertebrae bear the load. At ~60% strain, the lateral struts deform by Euler buckling, allowing the bony plates to slide past each other with relative ease. Once the plates reach the terminal corner of its lateral neighbor, they too begin to buckle (see dextral-ventral plate (red) in Fig. 3i). When compressed ventral-dorsally, the stress rise rate is slightly greater than in lateral compression (see Fig. 3a). In this direction (Fig. 3ii), the vertical struts buckle and the lateral struts bend downward in the direction of the sliding dorsal plates. The ventral plates slide over the dorsal plates and fan-out, while the dorsal plates slide under the ventral plates and buckle-in upon ventral-dorsal loading (see Fig. 3ii). There are two mechanisms that may add strength to the tail in the ventral-dorsal direction: (1) the vertical struts of the vertebrae are larger and more robust than the lateral struts, and (2) the vertical orientation of the hypaxial muscles may resist deformation when loaded parallel to the myomere orientation. Compression of the seahorse tail in the lateral and ventral-dorsal directions do not result in brittle fracture, unlike many bony structures. Rather, the sliding motion of the bony plates, with most of the strain being accommodated by the extension of connective collagen fibers, protects the spinal column from permanent damage. Fig. 3iii and 3iv show the dorsal view of the bony plates and vertebrae of a tail section compressed distal-proximally. The strength of the tail section at ~60% strain in this direction is nearly four times the strength in the ventral-dorsal direction (see Fig. 3a). Fig. 3iii shows the anterior plates slide into the posterior plates. When compressed distal-proximally, the distal spines of the anterior plates do not deform, but slide beyond the proximal grooves of the posterior plates (refer to Fig. 2d). Instead, the vertebrae bear the majority of the load and bend in response to the distal-proximal loading. As seen in Fig. 3iv, the lateral vertebral struts detach from the bony plates on one side of the tail and buckle on the opposing side. Moreover, the vertebra-vertebra connections stay intact, suggesting that the bending deformation observed in Fig. 3iv is unlikely to cause permanent damage in the spinal column that could result in paralysis of the prehensile appendage.

In addition to the multi-component tail structure detailed in Fig. 2 and 3, the plates themselves are fracture resistant materials. The bony plates are inorganic/organic composites composed of approximately 45 wt% calcium phosphate, 38 wt% protein, and 17 wt% water, with an average surface hardness of 240 ± 70 MPa, which is constant along the length of the tail. Compared to human bone, composed of ~65 wt% mineral [17] and a hardness ranging from 527-764 MPa [18], seahorse bones have a lower mineral content and hardness. This results in relatively elastic bones with a higher toughness that can withstand large deformations without fracture. Still, the bony-plated armor must be sufficiently hard to withstand failure from impact. For comparison, the hardness of the armored fish *Arapaima gigas* fish scales, crab exoskeleton, and abalone nacre are 200-550 MPa [11], 250-950 MPa [12], and 1-5 GPa [13], respectively. Fig. 4 (center) shows the Vickers hardness distribution across different structural features of a single bony plate. The proximal groove (160 ± 50 MPa) is nearly 40% softer than the distal spine (260 ± 40 MPa), enabling it to absorb the stresses associated with joint movement. According to the micrographs in Fig. 4a and 4b, the proximal groove is porous, which may help dampen joint movement during prehensile activities. The ridge nodules on the outer tip of the bony plates are the hardest region of the bone (320 ± 30 MPa) and function as a hard, protective shield against high impact. The plate wings have an average hardness of 230 ± 50 MPa. The surface morphologies of the plate wings vary depending on whether the plate is on the outer or inner side of the plate-plate overlap (refer to Fig. 2c). The outer plate wing is supported by a single solid rod-like strut (Fig. 4c). The strut on the inner plate wing becomes branched into two or more smaller struts at the tip to provide structural reinforcement and a wider surface area for plate-plate attachment (Fig. 4d).

The micrographs shown in Fig. 4e-g reveal the architectural hierarchy of a bony plate. The plates have hollow microchannels (100-500 μm in diameter) running the length each plate wing and the distal spine that connect to a central hollow chamber beneath the ridge nodules (see Fig. 4e). An external layer of hard mineralized tissue (160-320 MPa) encases a soft organic interior (80-200 MPa) that surrounds the hollow microchannels. This type of structural gradient is similarly observed in other mineralized biological composites, such as mammalian bones, teeth, and antlers [19]. Local collapse of the hollow interior due to impact may help protect the overall tail structure from damage. A fracture surface of the distal spine (Fig. 4f) shows the orientation of structural fibers that surround microtubules (1-10 μm in diameter) containing cross-oriented bundles of mineralized collagen fibers with a characteristic periodicity of ~67 nm (Fig. 4g) [17]. Akin to other natural structural materials such as mammalian bones, teeth, antlers, horns and hooves, the directional alignment of structural fibers and the presence of microtubules cause the bony plates to be highly anisotropic, energy absorbent materials [19]. Collapse of the microtubules under certain loading conditions prevent the buckling of structural fibers and arrest crack propagation. This type of localized failure is an extrinsic toughening mechanism commonly found in bone that protects the integrity of the overall structure [20].

4. Conclusions

In conclusion, the bony-plated armor in the tail of seahorses is a multifunctional device that provides structural support, protection, and prehension. Upon compression, the overlapping bony plates slide past each other, allowing the tail to be compressed to nearly 50% its original length before any permanent damage occurs. Even after permanent deformation occurs (> 50% strain), the tail does not exhibit brittle fracture. Instead, it exhibits a plastic response, which is accompanied by Euler buckling and bending of the bony plates and vertebral struts. This unusual deformation behavior protects the tail segments and central vertebrae from fracture, as the majority of seahorse predators capture their prey by crushing - crabs using claws; rays using crushing plates; sea turtles and birds using beaks. In addition to the impressive structural mechanics of the prehensile appendage, micro-hardness tests showed a distribution of hardness across a single bony plate that is tailored to specific functions - harder on the outer surface for protection and softer at the overlapping joints for mobility. The unique hierarchical structure-property-function relationships revealed by the seahorse tail may serve as inspiration for future biomimetic devices, such as steerable catheters [10], earthquake resistant structures, flexible armor, controlled anchoring mechanisms, or prehensile robotics.

5. Acknowledgements

We would like to thank Leslee Matsushige, Phil Hastings, H.J. Walker and Fernando Nosratpour of Scripps Institute of Oceanography, UCSD, for providing the seahorse specimens, Ryan Anderson of CalIT2, UCSD, for help in SEM, and Esther Cory and Robert Sah of the Department of Bioengineering, UCSD, for guided analysis of the μCT scans. This work is supported by the National Science Foundation, Division of Materials Research, Ceramics Program Grant, 1006931.

References

[1] Meyers MA, Chen PY, Lin AYM, Seki Y. Biological materials: Structure and mechanical properties. Prog Mater Sci 2008;53:1-206.
[2] Bar-Cohen Y. Biomimetics: Biologically Inspired Technologies. Boca Raton: Taylor and Francis Group; 2006.
[3] Lazaris A, Arcidiacono S, Huang Y, Zhou JF, Duguay F, Chretien N, et al. Spider silk fibers spun from soluble recombinant silk produced in mammalian cells. Science 2002;295:472-6.
[4] Dickinson MH, Lehmann FO, Sane SP. Wing rotation and the aerodynamic basis of insect flight. Science 1999;284:1954-60.
[5] Lourie SA, Stanley HF, Vincent ACJ, Hall HJ, Pritchard JC, Casey SP, et al. Seahorses: An Identification Guide to the World's Species and their Conservation. London: Project Seahorse; 1999.
[6] Foster SJ, Vincent ACJ. Life history and ecology of seahorses: implications for conservation and management. J Fish Biol 2004;65:1-61.

[7] Consi TR, Seifert PA, Triantafyllou MS, Edelman ER. The dorsal fin engine of the seahorse (Hippocampus sp.). J Morphol 2001;248:80-97.
[8] Ashley-Ross MA. Mechanical properties of the dorsal fin muscle of seahorse (Hippocampus) and pipefish (Syngnathus). J Exp Zool 2002;293:561-77.
[9] Hale ME. Functional morphology of ventral tail bending and prehensile abilities of the seahorse, Hippocampus kuda. J Morphol 1996;227:51-65.
[10] Praet T, Adriaens D, Cauter SV, Masschaele B, Beule MD, Verhegghe B. Inspiration from nature: dynamic modelling of the musculoskeletal structure of the seahorse tail. International Journal for Numerical Methods in Biomedical Engineering 2012.
[11] Lin YS, Wei CT, Olevsky EA, Meyers MA. Mechanical properties and the laminate structure of Arapaima gigas scales. Journal of the Mechanical Behavior of Biomedical Materials 2011;4:1145-56.
[12] Chen PY, Lin AYM, McKittrick J, Meyers MA. Structure and mechanical properties of crab exoskeletons. Acta Biomater 2008;4:587-96.
[13] Barthelat F, Li CM, Comi C, Espinosa HD. Mechanical properties of nacre constituents and their impact on mechanical performance. Journal of Materials Research 2006;21:1977-86.
[14] Webb PW, Hardy DH, Mehl VL. The effect of armored skin on the swimming of longnose gar, lepisosteus-osseus. Can J Zool-Rev Can Zool 1992;70:1173-9.
[15] Bruet BJF, Song JH, Boyce MC, Ortiz C. Materials design principles of ancient fish armour. Nat Mater 2008;7:748-56.
[16] Long JH, Hale ME, McHenry MJ, Westneat MW. Functions of fish skin: Flexural stiffness and steady swimming of longnose gar Lepisosteus osseus. J Exp Biol 1996;199:2139-51.
[17] Dorozhkin SV, Epple M. Biological and medical significance of calcium phosphates. Angew Chem-Int Edit 2002;41:3130-46.
[18] Rho JY, Tsui TY, Pharr GM. Elastic properties of human cortical and trabecular lamellar bone measured by nanoindentation. Biomaterials 1997;18:1325-30.
[19] McKittrick J, Chen PY, Tombolato L, Novitskaya EE, Trim MW, Hirata GA, et al. Energy absorbent natural materials and bioinspired design strategies: A review. Materials Science and Engineering: C 2010;30:331-42.
[20] Launey ME, Buehler MJ, Ritchie RO. On the Mechanistic Origins of Toughness in Bone. In: Clarke DR, Ruhle M, Zok F, editors. Annual Review of Materials Research, Vol 40. Palo Alto: Annual Reviews; 2010. p. 25-53.

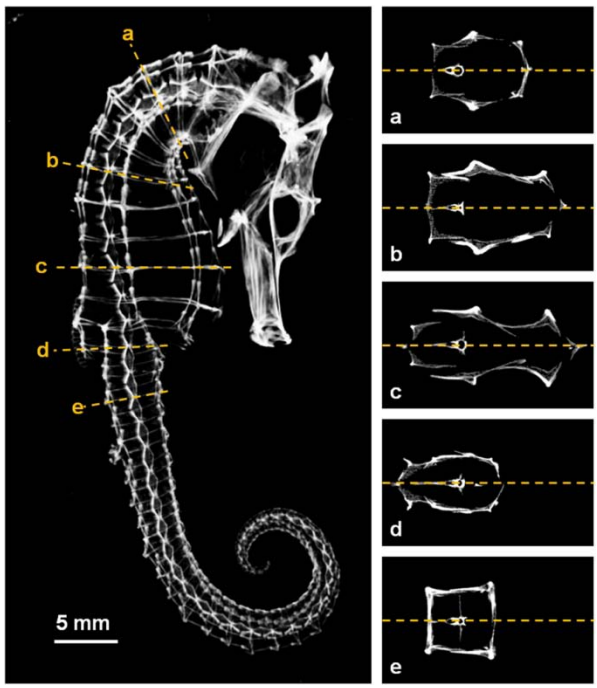

Fig. 1. µCT scan of a seahorse skeleton (*Hippocampus kuda*) illustrating the cross-sections of several different segments along the length of the fish: **(a-c)** heptagonal segments at different locations of the torso; **(d)** hexagonal segment at the dorsal fin (torso-tail intersection); **(e)** square-like segment of the prehensile tail.

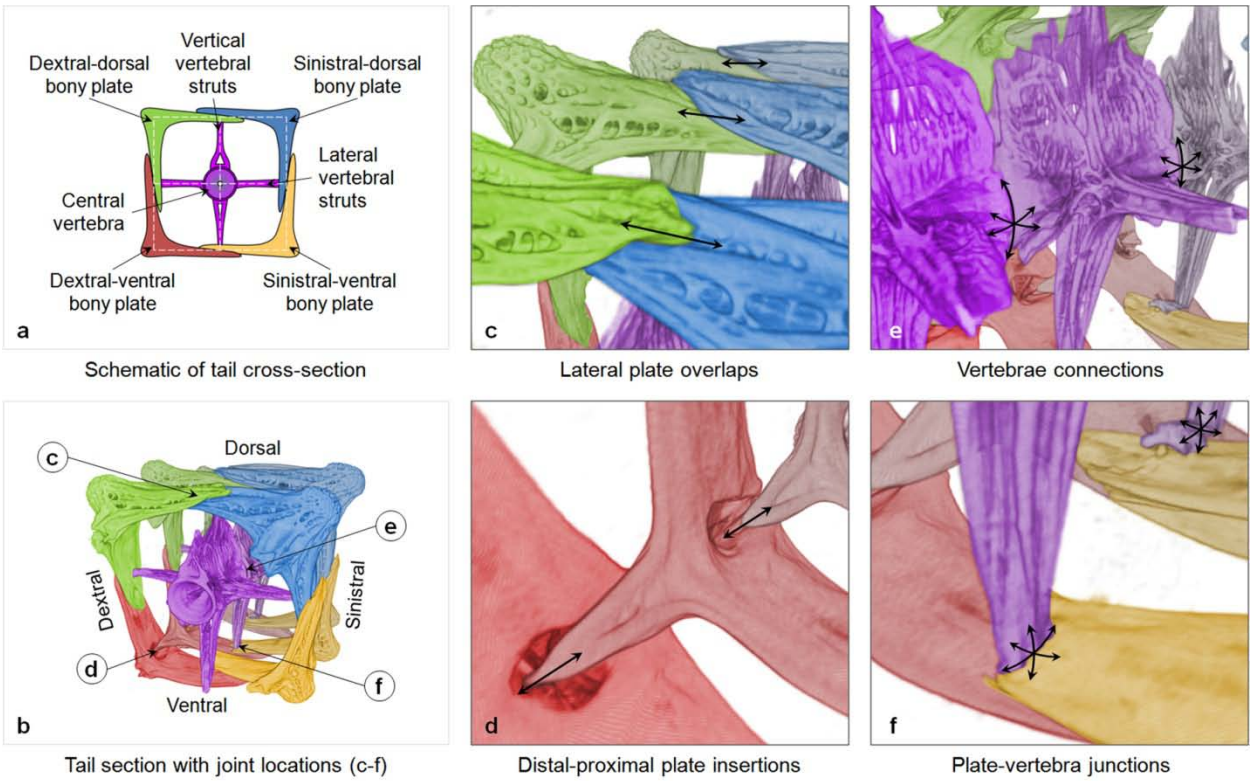

Fig. 2. (a) Schematic of a seahorse tail cross-section, denoting each bony component; **(b)** µCT image of a tail section (three bony segments) illustrating the four different joints: **(c)** gliding lateral plate overlaps; **(d)** gliding distal-proximal plate insertions; **(e)** pivoting vertebrae connections; **(f)** pivoting plate-vertebra junctions. Arrows indicate the directions of translational **(c, d)** and rotational **(e, f)** degrees of freedom. All µCT images were colored for clarity with Jasc Paint Shop Pro.

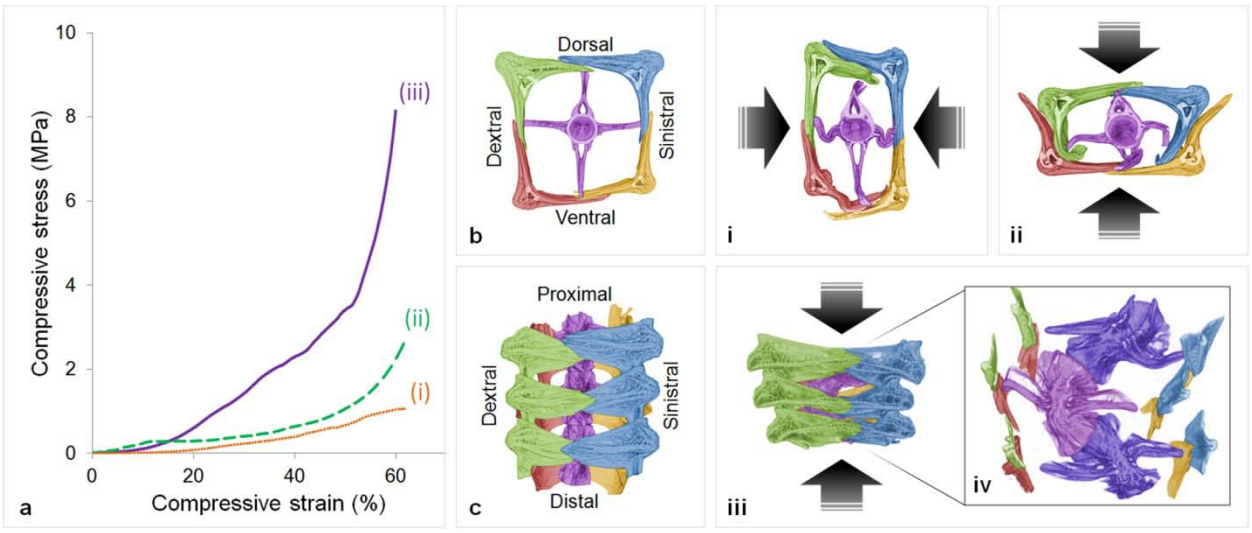

Fig. 3. (a) Stress-strain curves of three different seahorse tail sections (three bony segments each) compressed to ~60% strain: **(i)** laterally (dextral-sinistrally), **(ii)** ventral-dorsally, and **(iii)** distal-proximally. µCT images: **(b)** distal view of tail cross-section before compression; **(c)** dorsal view of tail section (three segments) before compression; **(i)** distal view of tail cross-section compressed laterally; **(ii)** distal view of tail cross-section compressed ventral-dorsally; **(iii)** dorsal view of tail section (three segments) compressed distal-proximally; **(iv)** magnified cutaway of image **(iii)** showing vertebrae bending due to distal-proximal loading. Sample dimensions were measured and rounded to the nearest 0.5 mm to approximate the compressive stress-strain curves. All samples were compressed to ~60% strain. All µCT images were colored for clarity with Jasc Paint Shop Pro.

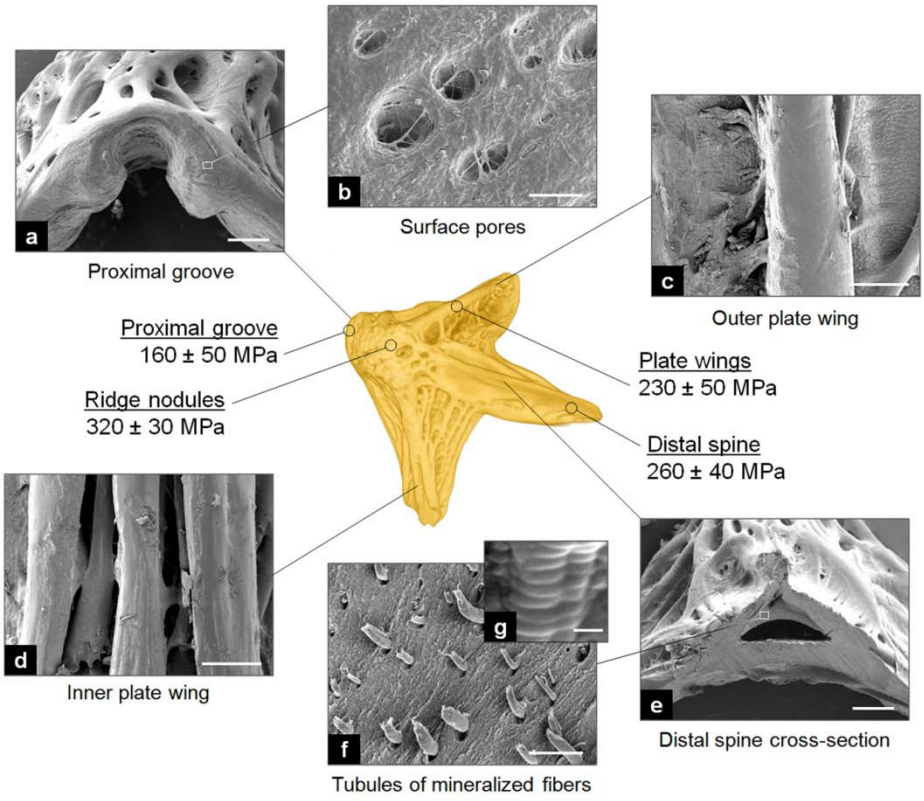

Fig. 4. Architectural hierarchy and micro-hardness distribution of a bony plate. **(Center)** µCT image of a single bony plate, showing the Vickers micro-hardness at four different locations: proximal groove (160 ± 50 MPa), ridge nodules (320 ± 30 MPa), plate wings (230 ± 50 MPa), and distal spine (260 ± 40 MPa). SEM micrographs: **(a)** rounded architecture of the proximal groove; **(b)** surface pores on the proximal groove; **(c)** reinforcing rod-like strut on the outer plate wing; **(d)** reinforcing branched struts on the inner plate wing; **(e)** cross-section of distal spine showing a hollow microchannel; **(f)** fracture surface of distal spine showing microtubules containing bundles of mineralized organic fibers; **(g)** mineralized collagen fibril exhibiting characteristic periodicity (~67 nm). Scale bars: (a) 250 µm; (b) 10 µm; (c) 200 µm; (d) 200 µm; (e) 250 µm; (f) 10 µm; (g) 200 nm.